Electronic Supplementary Information

Enhanced activity and stability of polymeric carbon nitride photoanodes by yttrium incorporation

Sanjit Mondal,[a] Ayelet Tashakory,[a] Gabriel Mark,[a] Shmuel Barzilai,[b] Angus Pedersen,[c] Michael Volokh,[a] Josep Albero,[d] Hermenegildo García,[d] Menny Shalom[a]*

[a] Department of Chemistry and Ilse Katz Institute for Nanoscale Science and Technology, Ben-Gurion University of the Negev, Beer-Sheva 8410501, Israel.

[b] Department of Chemistry Nuclear Research Centre-Negev P.O. Box 9001, Beer-Sheva 84910, Israel

[c] Department of Chemical Engineering, Imperial College London, London SW7 2AZ, England

[d] Instituto Universitario de Tecnología Química CSIC-UPV, Universitat Politècnica de València, València 46022, Spain.

Corresponding author E-mail: mennysh@bgu.ac.il

Detailed Experimental Procedures

Materials

Yttrium acetate tetrahydrate ($Y(OAc)_3 \cdot 4H_2O$, ≥ 99%) and melamine (99%) were purchased from Sigma-Aldrich. Disodium phosphate (Na_2HPO_4, 98+%) and sodium dihydrogen phosphate (NaH_2PO_4, 96%) were purchased from Alfa Aesar. Ethylene glycol (EG, ≥ 99.5%) was bought from Merck. Ethanol (≥ 99.9%), sulfuric acid (H_2SO_4, 98% w/w, AR grade), and acetone (99.5%) were purchased from Bio-Lab Ltd, Israel. Anhydrous sodium sulfate (Na_2SO_4, 99%), and potassium hydroxide pellets (KOH, 85% w/w, AR grade) were purchased from Loba Chemie, India. Triethanolamine (TEOA, ≥ 99.0%) was purchased from Glentham, UK. Fluorine-doped tin-oxide (FTO)-coated glass (12–14 Ω sq^{-1}) was bought from Xop Glass Company, Spain. Graphene oxide (GO, 0.4% w/w, > 95%) aqueous suspension was brought from University Wafer Inc., USA. In addition, deionized (DI) water with 18.2 MΩ cm resistivity was obtained using a Millipore Direct-Q3 water purification system. All chemicals were used as received without further purification.

Preparation of a CNGO film over FTO as a photoanode

A porous CN film with embedded reduced graphene oxide (CNGO) over fluorine-doped tin oxide coated glass (conductive substrate; referred to as FTO) was prepared as an electrode. 1 g melamine powder and 0.5 mL graphene oxide (GO, 0.8% w/w, obtained through the concentration *via* heating of 0.4% w/w GO aqueous suspension at 55 °C) mixture were dispersed using ethylene glycol (0.6 mL) into a paste that was doctor-bladed over the FTO, in line with previous publications. The precursor films were dried on a hot plate at ca. 75 °C for 30 minutes. A porous CNGO film was obtained after calcination of the precursor films over

FTO in closed (not sealed) glass tubes at 550 °C for 4 h under a constant N_2 flow in a tube furnace.

Modification of CNGO films with Y-clusters for Y-CNGO photoanode preparation

At first, melamine (10 g) and yttrium acetate (in three distinct loading amounts: 0.25, 0.50, and 0.75 mmol), were dispersed in an ethanol:water mixture (1:1 v/v, *i.e.*, volume ratio). This mixture was agitated at 300 rpm and 55 °C for 8 h in an open beaker on a hot plate. The resultant powder served as the precursor for film fabrication. This Y-incorporated precursor powder served to form the photoanodes described in section 4.2 (1 g precursor powder, 0.5 mL of 0.8 wt% GO, and 0.6 mL of EG formed a viscous paste doctor-bladed onto an FTO substrate). Subsequent calcination (550 °C for 4 h under N_2 atmosphere) yielded a film of yttrium cluster incorporated porous nanosheets interconnected with twisted nanotubes.

Characterization

The structural analysis of synthesized photoelectrodes was performed using powder X-ray diffraction patterns (XRD) recorded using a PANalytical's Empyrean diffractometer, equipped with a position-sensitive detector X'Celerator. Data was recorded with a scanning time of ~15 min for 2ϑ ranging from 10° to 60° using Cu Kα radiation (λ = 1.54178 Å, 40 kV, 30 mA).

Fourier-transform infrared spectroscopy (FTIR) was carried out to study the functional groups of the electrode materials on a Thermo Scientific Nicolet iS5 FTIR spectrometer (equipped with a Si attenuated total reflectance (ATR) accessory).

X-ray photoelectron spectroscopy (XPS) measurements were performed on a Thermo Scientific ESCALAB 250 (Al Kα, 1486.6 eV) with an applied pass energy of 20 eV.

UV–vis absorption and steady-state photoluminescence (PL) spectroscopies were used to study the optical properties of the electrode materials. A Cary 100

spectrophotometer, in a double-beam configuration using two 10 mm quartz cuvettes for liquids (UV–vis absorbance) or equipped with a diffuse reflectance accessory (DRA) for powder and films diffuse reflectance spectroscopy (DRS) was used. A Horiba Scientific FluoroMax 4 spectrofluorometer was used for steady-state PL spectroscopy.

The valence band (VB) maximum energy was estimated using XPS measurements in a Thermo Scientific ESCALAB Xi^+ with a HeI excitation source.

The morphology of the supramolecular precursor and the final photoelectrodes were characterized by scanning electron microscopy (SEM) using an FEI Verios ultrahigh-resolution SEM, equipped with a FEG source and a through-lens detector (TLD), operated at U_0 = 3.5 kV and I = 25 pA; to avoid charging effects, some samples were sputtered with ≤ 5 nm Au-Pd alloy using a Quorum Q150T ES system.

High-angle annular dark-field scanning transmission electron microscopy (HAADF-STEM) images were recorded using S/TEM Spectra 200 microscope (U_0 = 200 kV; X-CFEG source).

For time-of-flight secondary ion mass spectrometry (ToF-SIMS) measurements, an ION-TOF V (IONTOF GmbH, Germany) was used for both before ('Fresh) and after ('*post-mortem*') operation, *i.e.*, stability testing as shown in Fig. 5 in the manuscript for samples that were measured on their FTO substrate. The ToF-SIMS measurements employed a 100 µm × 100 µm field of view using a Bi^{3+} primary ion beam with 25 keV and 0.4 pA beam current and 128 × 128 pixels. The measurements were rastered in sawtooth mode, with 100 µs cycle time (870 amu), employing a 5 µm spot size. Positive polarity was used based on previous yttrium ToF-SIMS reports.[1] The sputter beam consisted of a 11 nA Ar beam (~1600 cluster size) at 10 keV rastered over 500 µm × 500 µm, with non-interlaced 1 sputter frames and 1 s pause, up to a dose density of 10^{16}–10^{17} ions cm^{-2}. The flood gun was on during measurements. Spectra

were calibrated to: C^-, CH^+, CH_2^+, CH_3^+, $C_2H_3^+$, $C_3H_5^+$, $C_4H_7^+$, and $YN_2C_2^+$, with deviation <50 ppm for all calibration peaks in the samples. Data analysis was performed using SurfaceLab 7 software, and normalization of peak intensity counts was computed based on the total ion count across the measured spectrum. All identified peaks in the samples possessed <100 ppm deviation from calculated atomic mass units and resolution <8000 mass units. The measurement procedure was repeated at two different sample locations.

Transient absorption spectroscopy (TAS) experiments were carried out in quartz cuvettes (10 mm optical length) containing N_2-saturated dispersions of the samples in acetonitrile with A = 0.8 at 300 nm. The experiments were carried out using an OPO system Ekspla (EKS-NT342C-10) coupled with a UV extension (EKS-NT342C-SH-SFG) as the excitation source and an Edinburgh Instruments detection system (LP980) coupled with an ICCD camera (Andor iStar CCD 320 T).

PEC and electrochemical measurements

All the photoelectrochemical measurements were carried out using a standard three-electrode system on a single-channel PalmSens4 potentiostat (PalmSens, Netherlands). A Pt foil (1.0 cm^2) and Ag/AgCl (saturated KCl) were used as the counter and reference electrodes, respectively. 0.10 M KOH aqueous solution (pH ~13.1) or 0.1 M KOH aqueous solution containing 10% v/v triethanolamine (TEOA; serving as a hole scavanger) were used as the electrolyte for the photocurrent experiments. Additionally, a NaH_2PO_4/Na_2HPO_4 aqueous solution (pH 7, I = 0.10 M) and 0.50 M H_2SO_4 (pH ~0.3) aqueous solutions were also used for photocurrent measurements in neutral and acidic environments, respectively. The measured potentials ($V_{Ag/AgCl}$) were converted to the reversible hydrogen electrode (RHE) scale (V_{RHE}) using the following equation:

$$V_{RHE} = V_{Ag/AgCl} + 0.0591 \times pH + 0.197\ V \quad \text{(Eq. S1)}$$

The reported photocurrent density of all photoanodes is reported following measurement at a bias potential of V_{RHE} = 1.23 V under 1 sun illumination (power density of ~100 mW cm^{-2}) supplied by a Newport LCS-100 solar simulator (100 W Xe lamp and an integrated AM 1.5 filter, calibrated using a Newport 919P power meter). All PEC measurements were taken at consistent intervals of 20 seconds, alternating between light-on and light-off conditions (manual illumination chopping during chronoamperometric measurement). Linear sweep voltammetry (LSV) measurements were performed in the dark and under 1 sun illumination in the range V_{RHE} = 0–1.8 V.

For incident photon-to-current conversion efficiency (IPCE) measurements, a Zahner CIMPS-QE/IPCE photoelectrochemical workstation coupled with a TLS03 tunable light source controlled by a PP211 potentiostat (Zahner-Elektrik, Germany) in a dedicated three-electrode photoelectrochemical cell (PEEC-2) using an Ag/AgCl (sat. KCl) reference electrode and Pt coil as the counter electrode was used. The IPCE calculations were performed using the following equation:

$$IPCE\ (\%) = \frac{J \times 1240}{\lambda \times I_{incident}} \times 100\% \quad \text{(Eq. S2)}$$

Where J is the photocurrent density in units of mA cm^{-2}, 1240 is the units conversion factor, $I_{incident}$ is the incident illumination power in units of mW cm^{-2} (calibrated to illumination spot of 8 mm in diameter) of the specific monochromatic LED illumination wavelength (λ is measured in nm). The calculation was performed using the coupled ThalesXT software.

Mott–Schottky analysis was performed in 0.50 M Na_2SO_4 aqueous solution using an Autolab potentiostat (PGSTAT302N, Metrohm, Switzerland). The carrier concentration (N_D)

was calculated from a Mott–Schottky analysis at a 1 kHz frequency using the following equation:

$$N_D = \frac{2}{ne\varepsilon\varepsilon_0} \quad \text{(Eq. S3)}$$

Where n is the slope of the linear part of the C^{-2} *vs.* V_{RHE} plot, e = 1.602 × 10^{-19} C (electron charge), ε_0 = 8.860 × 10^{-12} F m^{-1} (vacuum permittivity), and ε = 9.801 (relative permittivity) for the photoanode material (*i.e.*, polymeric carbon nitride).

Electrochemical impedance spectroscopy (EIS) measurements in 0.5 M Na_2SO_4 aqueous solution, using a three-electrode configuration, were used to measure the complex impedance of the photoanodes in the dark (films over FTO). The Nyquist plots represent measurements at applied potentials (V_{RHE}) of 0.05, 0.10, 0.15, and 0.25 V over a frequency range from 50 kHz to 100 mHz using PalmSens4 potentiostat (PalmSens, Netherlands).

Evolved gas quantification during water-splitting experiments: Oxygen (O_2) generation for CNGO and CNGO-0.50 Y films in 0.1 M KOH solution was detected using a fiber optic oxygen meter (Firesting GmbH, Germany) under chronoamperometric conditions (V_{RHE} = 1.23 V, 1 sun illumination) in a two-compartment cell (H-cell). The H-cell was tightly sealed with a rubber septum and parafilm to avoid gas leakage. The electrolyte solution was purged with Ar (99.999%) for 30 min before the experiments. The O_2 quantification was performed for a duration of 1 hour; the presented data underwent a background subtraction processing. For H_2 quantification, 100 µL sample of gas was taken every 20 min with an A-2 Luer lock gas syringe (Pressure-lok precision analytical syringe from VICI), sampling from the headspace and injected into a gas chromatograph (Agilent 7820 GC system), equipped with a CP-Molsieve 5A column.

The Faradaic efficiency (FE) was calculated using Eq. S4–S5:

$$n = \frac{I \times t}{z \times F} \qquad \text{(Eq. S4)}$$

Where *n* is the gas amount (mol), *I* is the current (A), *z* is the number of transferred electrons (for O_2 (OER) *z* = 4; for H_2 (HER) *z* = 2), *t* is the time (s), and *F* is the Faraday constant (96,485 C mol^{-1}).

The theoretical amount of O_2/H_2 was calculated from Faraday' 's law, Eq. S5:

$$FE\ (\%) = \frac{Experimental\ evolved\ gas\ amount}{Theoretical\ evolved\ gas\ amount} \times 100\% \qquad \text{(Eq. S5)}$$

Where the evolved gasses (O_2 and H_2) are quantified in µmol.

Electronic Supplementary Information Figures and Tables

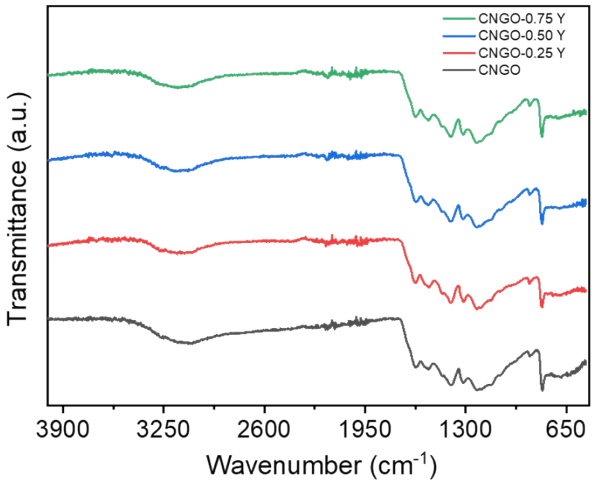

Fig. S1. FTIR spectra of the CNGO and Y-cluster-modified CNGO films. The transmittance spectra are vertically offset for clarity.

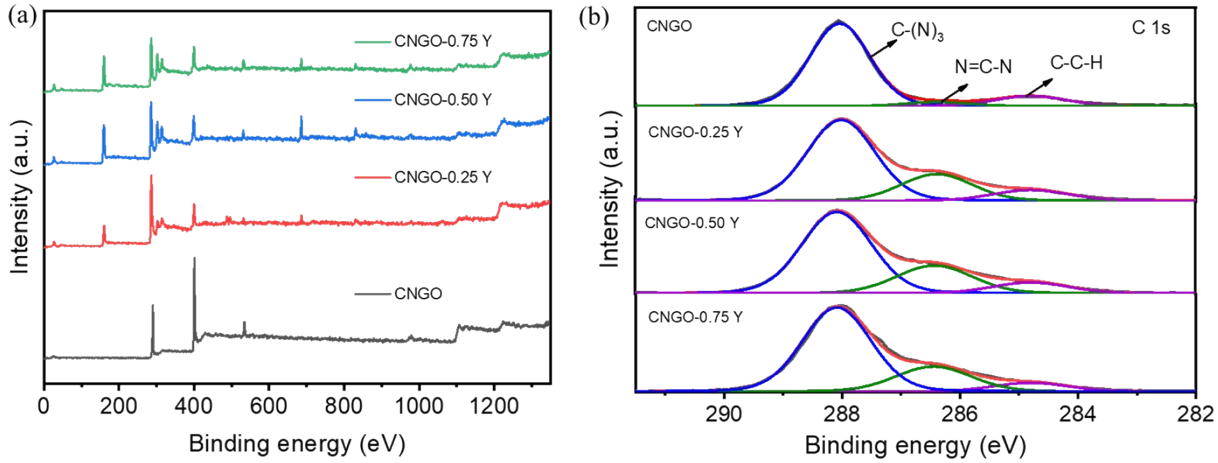

Fig. S2. XPS analysis of CNGO and Y-cluster-modified CNGO films. (a) survey spectra, (b) high-resolution C 1s spectra, with three deconvoluted peaks for each spectrum. The spectra are vertically offset for clarity.

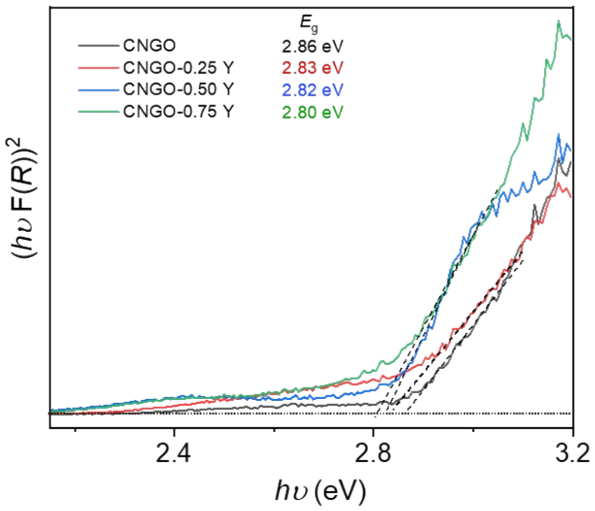

Fig. S3. Tauc plot of the CNGO and Y-cluster-modified CNGO films, assuming a direct optical band gap (E_g); the calculated E_g values are listed in the legend.

Note S1.

The XPS valence band values on the normal hydrogen electrode scale (NHE) of the electrodes were calculated using Eq. S6:

$$E_{NHE}\,(V) = \Phi + E_{VB\text{-}XPS} - 4.44 \qquad \text{(Eq. S6)}$$

Where Φ is the work function of the instrument (Φ = 4.84 eV), $E_{VB\text{-}XPS}$ is the experimentally determined valence band position, and 4.44 eV is the vacuum level.

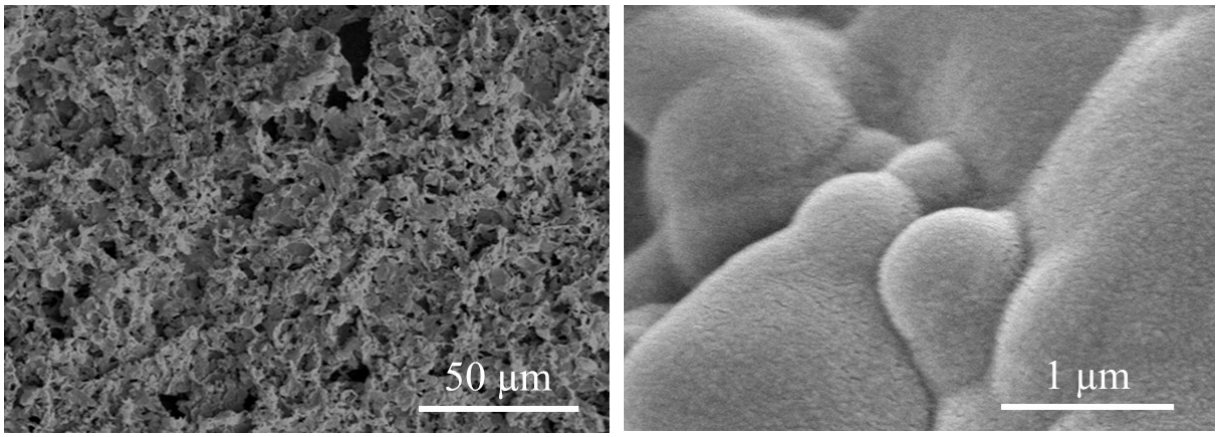

Fig. S4. SEM images of bare CNGO film at two magnifications.

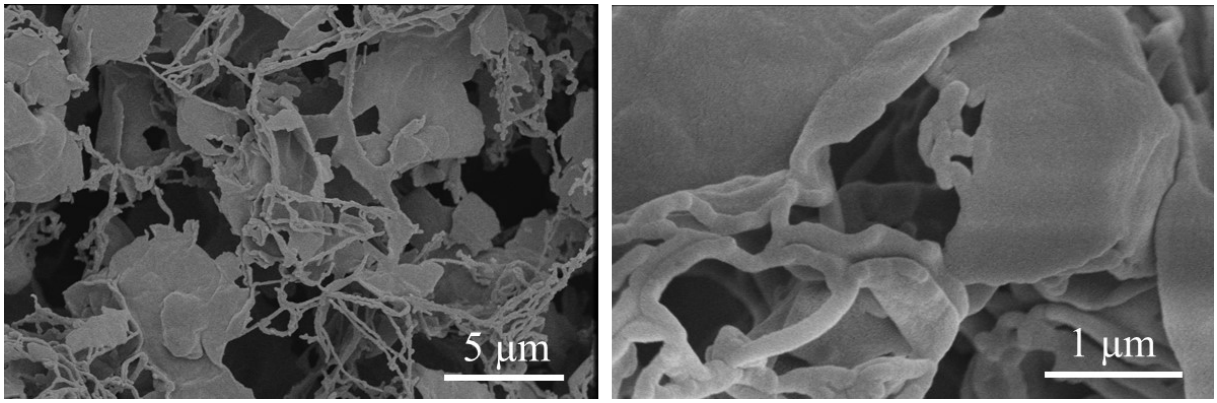

Fig. S5. SEM images of CNGO-0.25 Y film at two magnifications.

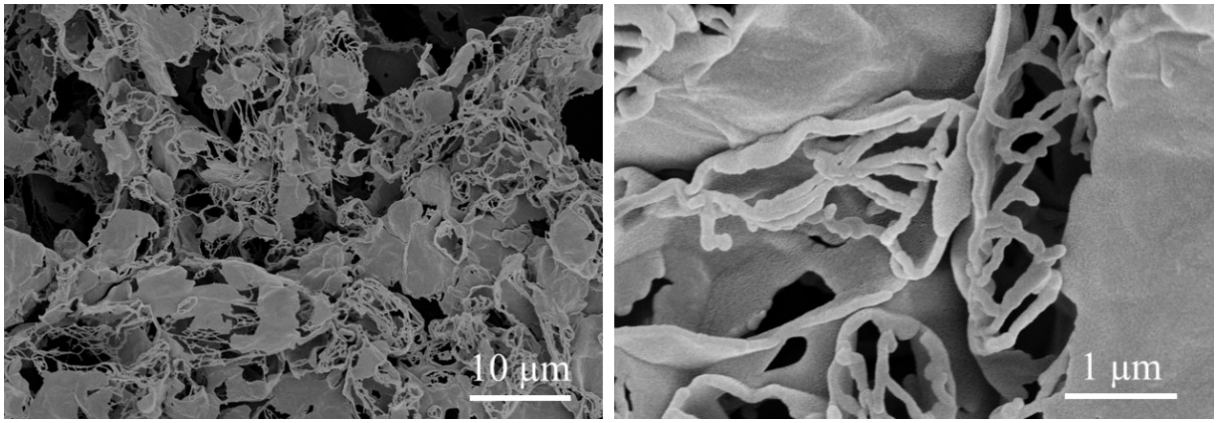

Fig. S6. SEM images of CNGO-0.75 Y film at two magnifications.

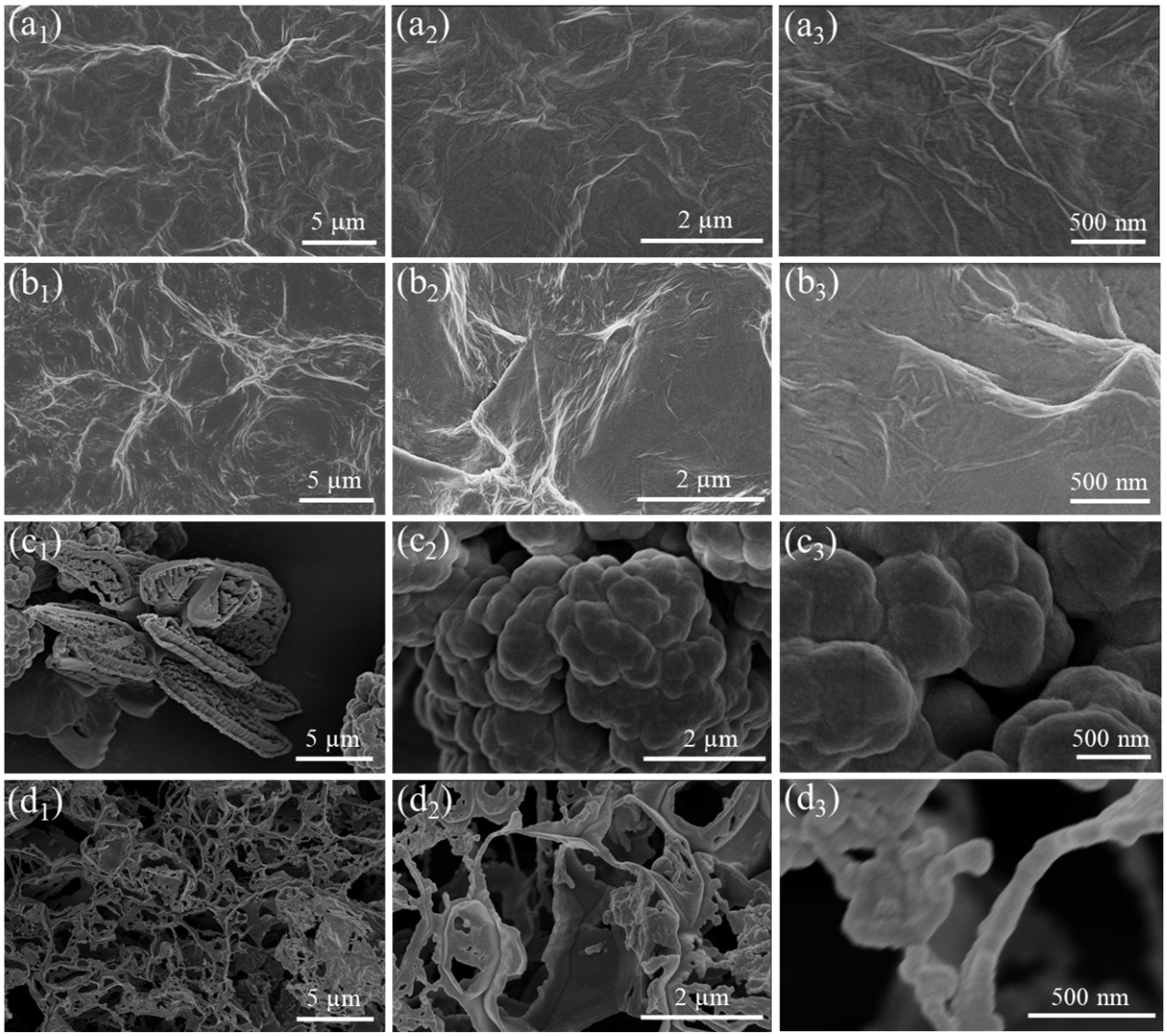

Fig. S7. SEM images of films obtained by calcination of different precursors over FTO for 4 h at 550 °C under N_2 flow. (a_1–a_3) rGO films obtained by calcination of GO only. (b_1–b_3) Y-rGO film obtained by calcination of a GO and yttrium acetate. (c_1–c_3) CN film obtained by calcination of melamine. (d_1–d_3) Y-cluster-modified CN film obtained by calcination of melamine and yttrium acetate.

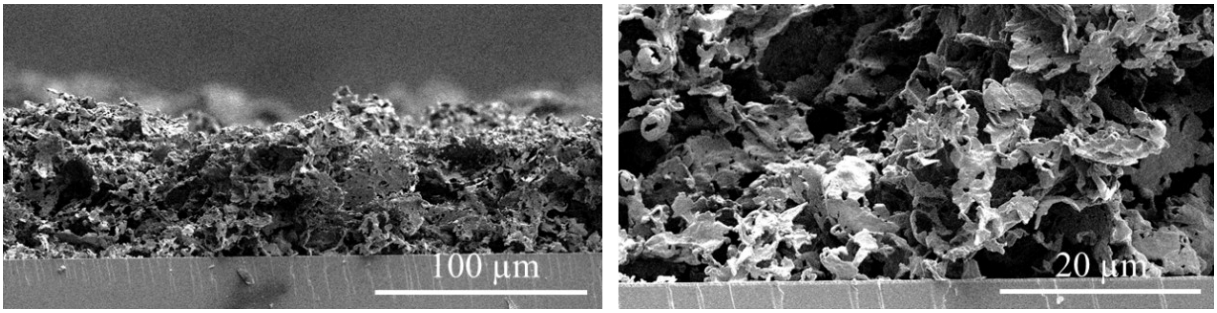

Fig. S8. Cross-sectional SEM images of a bare CNGO film over an FTO substrate.

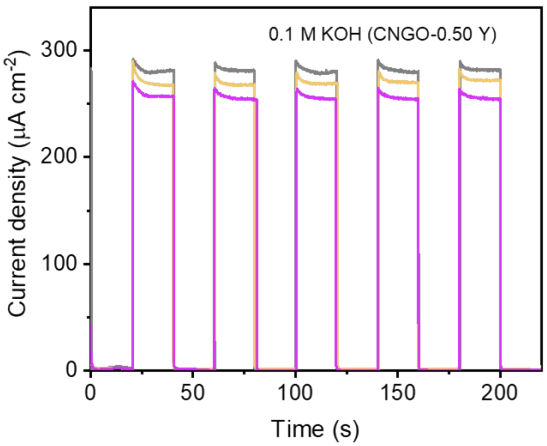

Fig. S9. Three sets of chronoamperometry measurements obtained in 0.1 M KOH at V_{RHE} = 1.23 V for CNGO-0.50 Y films assessing photocurrent density under 1 sun illumination on/off cycles).

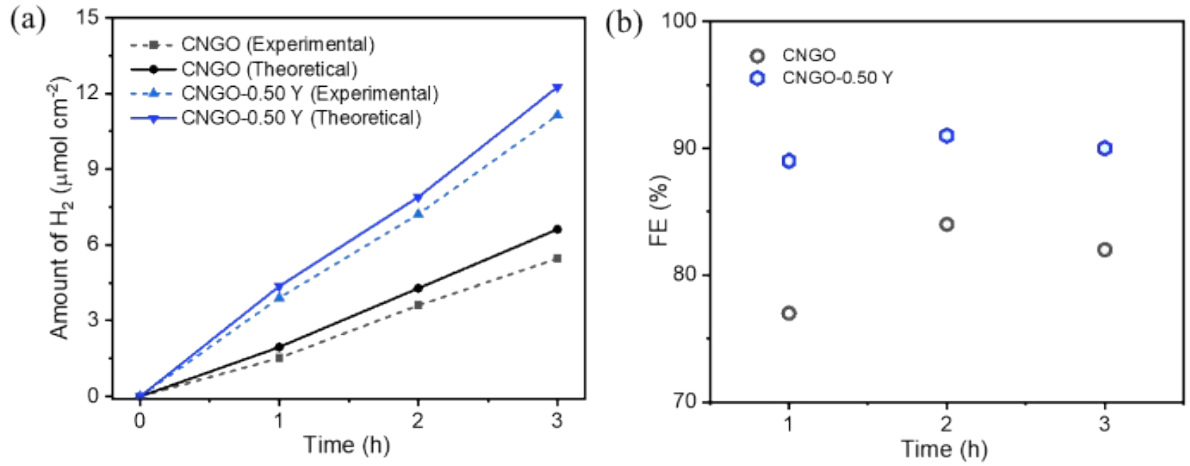

Fig. S10. Evolved H_2(g) quantification. (a) H_2 production using pristine CNGO and CNGO-0.50 Y films as the photoanodes (*i.e.*, experimental values) and the theoretical expected values from the current density (chronoamperometry experiment), both normalized to the photoanode's geometrical active area. (b) The corresponding calculated HER FE plot.

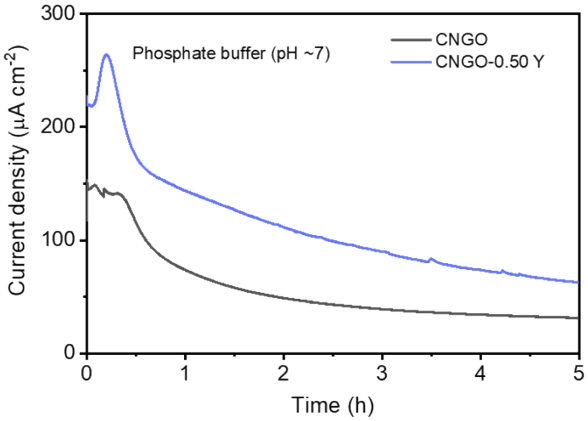

Fig. S11. Stability in a neutral electrolyte (phosphate buffer, pH ~7) for bare CNGO and CNGO-0.50 Y films under constant 1 sun illumination.

Table S1. CN-based photoanodes used for the oxygen evolution reaction (PEC water-splitting).

Material	Electrolyte	Photocurrent density at V_{RHE} = 1.23 V	Illumination	Stability measurement period	OER FE (%)	Reference
CNGO-Y	0.1 M KOH	275 μA cm^{-2}	100 mW cm^{-2}, AM1.5G	10 h	90%	This work
3MelM$_{680/10}$	0.1 M KOH	120 μA cm^{-2}	100 mW cm^{-2}, AM1.5G	20 h	36%	[2]
CN$_{M\text{-}HCl(HT)}$	0.1 M KOH	183 μA cm^{-2}	100 mW cm^{-2}, AM1.5G	10 h	92%	[3]
CN-CMK-*s*-MeOH	0.1 M KOH	139 μA cm^{-2}	100 mW cm^{-2}, AM1.5G	5 h	_	[4]
S-doped PCN/Bi_2WO_6	0.1 M KOH	57 μA cm^{-2}	100 mW cm^{-2}, AM1.5G	10 min	_	[5]
CNGO-ZnSe NRs	0.1 M KOH	160 μA cm^{-2}	100 mW cm^{-2}, AM1.5G	12 h	87%	[6]
β-FeOOH/CN	0.1 M NaOH	320 μA cm^{-2}	100 mW cm^{-2}, AM1.5G	1 h	_	[7]
CN-MeM/M$_{0.20}$	0.1 M KOH	133 μA cm^{-2}	100 mW cm^{-2}, AM1.5G	9 h	_	[8]
CN-Ru$_{15}$	Phosphate buffer	180 μA cm^{-2}	100 mW cm^{-2}, AM1.5G	5.5 h	89%	[9]
PCN	0.1 M NaOH	140 μA cm^{-2}	100 mW cm^{-2}, AM1.5G	2 h	_	[10]
Porous CN/rGO	0.1 M KOH	125 μA cm^{-2}	100 mW cm^{-2}, AM1.5G	_	_	[11]
CN nanolayer	0.1 M Na_2SO_4	210 μA cm^{-2}	100 mW cm^{-2}, AM1.5G	_	_	[12]
Ni-CN_x	0.1 M KOH	70 μA cm^{-2}	100 mW cm^{-2}, AM1.5G	0.33 h	_	[13]
CuO/CN	0.1 M KOH	172 μA cm^{-2}	100 mW cm^{-2}, AM1.5G	_	40%	[14]
g-CN/SnO_2	0.5 M Na_2SO_4	150 μA cm^{-2}	100 mW cm^{-2}, AM1.5G	1 h	_	[15]
Co/S g-C_3N_4/BiOCl	0.5 M Na_2SO_3 + $NaHCO_3$	393 μA cm^{-2}	100 mW cm^{-2}, AM1.5G	3 h	_	[16]
gCN@CuAF/$Ni(OH)_2$	0.5 M Na_2SO_4	320 μA cm^{-2}	100 mW cm^{-2}, AM1.5G	3 h	_	[17]
CoP/g-CN	0.5 M Na_2SO_4	150 μA cm^{-2}	100 mW cm^{-2}, AM1.5G	_	_	[18]
B and S doped CN	0.1 M KOH	900 μA cm^{-2}	100 mW cm^{-2}, AM1.5G	0.25 h	47%	[19]
CN-MR/$NiFeO_xH_y$	0.1 M KOH	320 μA cm^{-2}	100 mW cm^{-2}, AM1.5G	35 h	41%	[20]
CN-MSG/M	0.1 M KOH	270 μA cm^{-2}	100 mW cm^{-2}, AM1.5G	18 h	29%	[21]

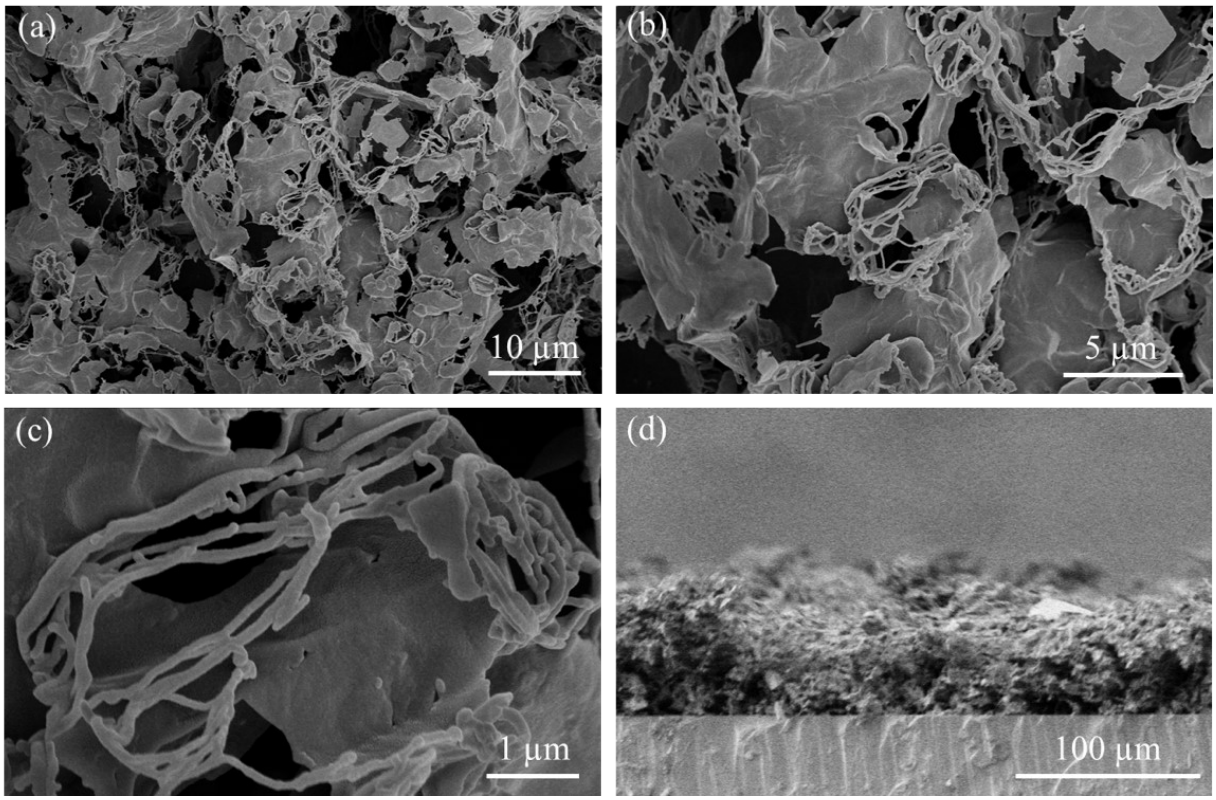

Fig. S12. SEM images of post-operation CNGO-0.50 Y photoanode after 30 h PEC activity (post-catalysis) in the presence of 10% v/v TEOA.

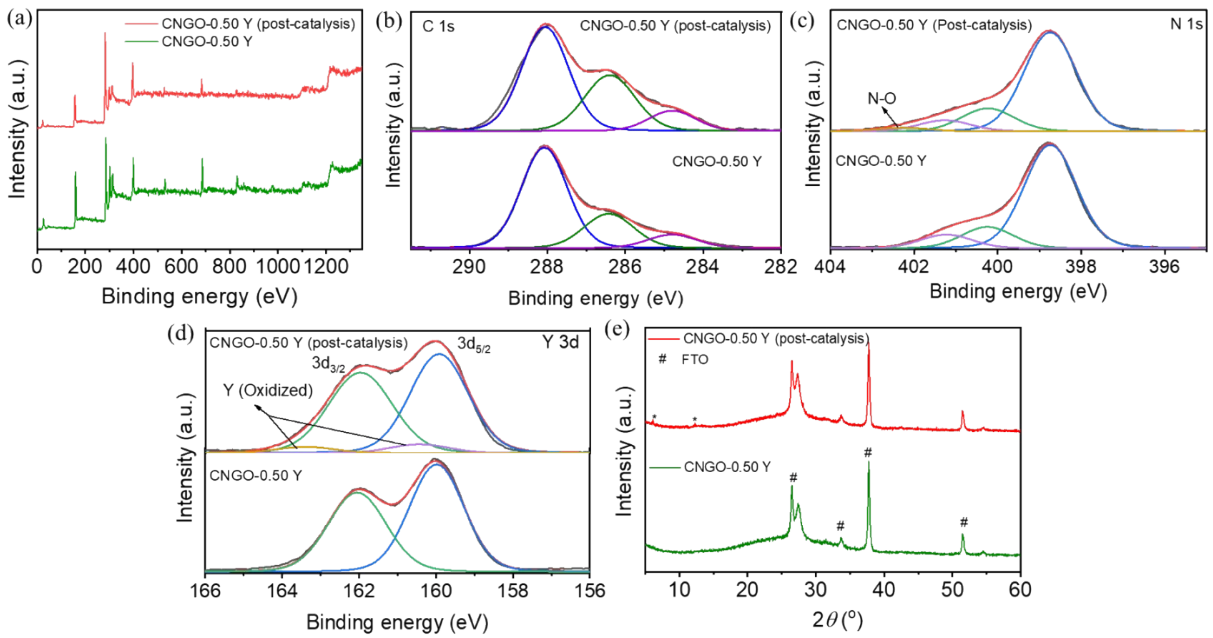

Fig. S13. XPS and XRD characterization of CNGO-0.50 Y photoanodes before and after 30 h PEC activity (post-catalysis) in the presence of 10% v/v TEOA. (a) XPS survey spectra, and high-resolution XPS spectra: (b) C 1s, (c) N 1s, and (d) Y 3d. (e) XRD pattern (some small unidentified peaks marked with '*' after the 30 h PEC study. The XPS spectra and XRD patterns are vertically offset for clarity.

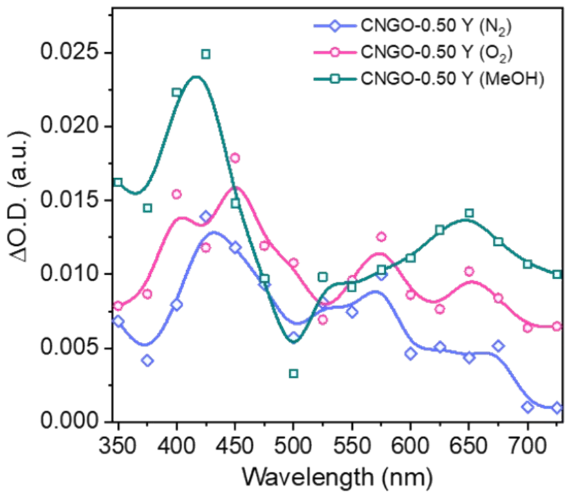

Fig. S14. Transient absorption spectra of CNGO-0.50 Y under different environmental conditions (N_2, O_2, and MeOH).

Table S2. Fitting parameters for the transient absorption decay presented in Fig. 4e of CNGO and CNGO-0.50 Y dispersions in MeCN under N_2 atmosphere, monitored at 650 nm (laser excitation at 355 nm). CNGO fitted to $F(t) = Ae^{-\tau t}$; CNGO-0.50 Y fitted to $F(t) = A_1e^{-\tau_1 t} + A_2e^{-\tau_2 t}$.

A	τ		
0.016	121.03 ns		
A_1	τ_1	A_2	τ_2
0.022	144.28 ns	24.74	2.5223 µs

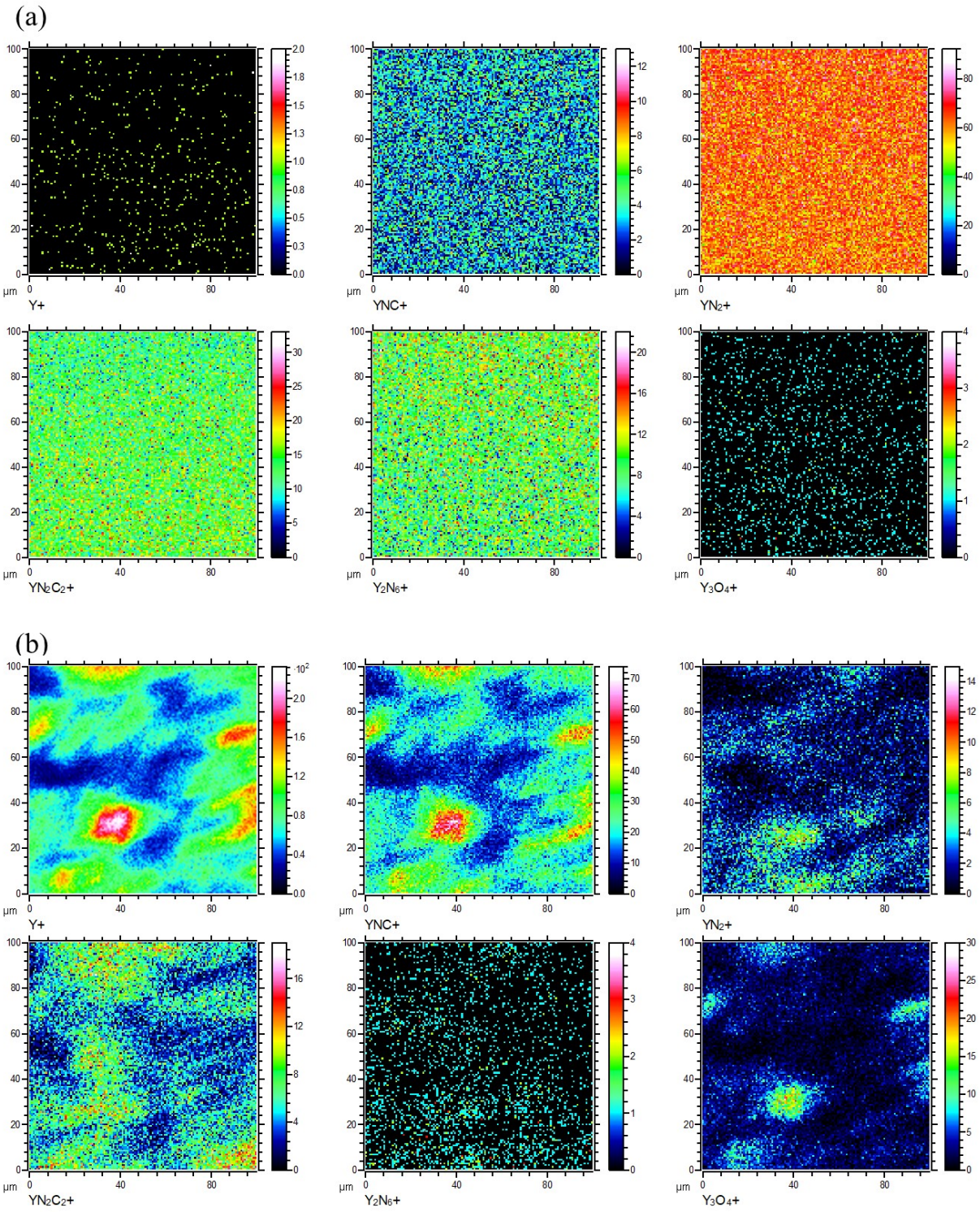

Fig. S15. Comparison of the distribution of positive fragment counts in ToF-SIMS over 100 µm × 100 µm field of view for fragments of Y^+, YNC^+, YN_2^+, $YN_2C_2^+$, $Y_2N_6^+$, and $Y_3O_4^+$ in (a) fresh and (b) *post-mortem* CNGO-0.50 Y electrodes. The right-hand scale bar indicate fragment counts.

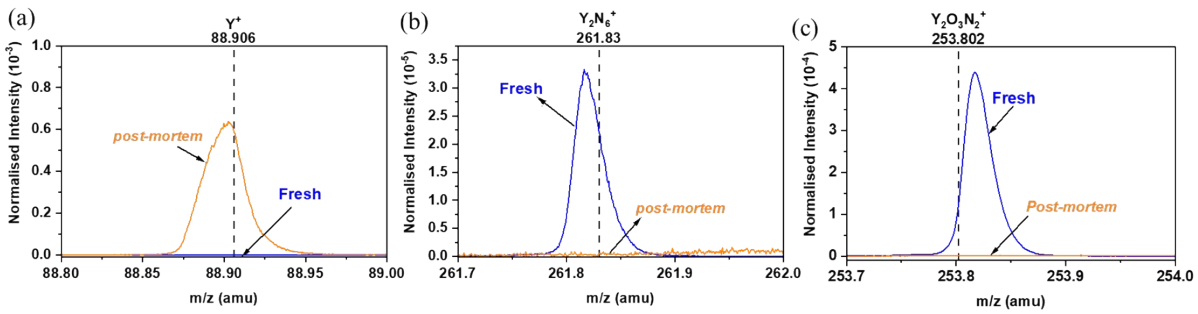

Fig. S16. ToF-SIMS of Y-based fragments before ('Fresh') and after electrochemical testing ('*post-mortem*') of CNGO-0.50 Y in positive SIMS spectrum shown for (a) Y^+, (b) $Y_2N_6^+$, and (c) $Y_2O_3N_2^+$.

DFT Methodology and Results

In this study, we employed density functional theory (DFT) to computationally investigate the interaction between yttrium (Y) and CN surfaces, calculated as ideal graphitic C_3N_4 surfaces. Based on the available experimental characterization, we considered a supercell model consisting of a single CN layer, arranged in a tri-*s*-triazine geometry, containing 24 carbon atoms and 32 nitrogen atoms, with a top vacuum layer. The initial slab structure was relaxed to determine the optimum lattice parameters and allow the atoms within the slab to adjust to their equilibrium positions. Fig. S17 illustrates the tri-*s*-triazine geometry of the carbon nitride model used in the study. The calculations were performed using the Quantum ESPRESSO software package,[22] with the supercell being subjected to periodic boundary conditions. To identify the preferred adsorption sites of the Y atoms on the carbon nitride surface and to compute the corresponding adsorption energies, all the atoms in the supercell were allowed to relax. For selected relaxed configurations, the electronic properties were subsequently computed. The adsorption energy (E_{ads}) was calculated according to the following equation:

$$E_{\text{ads}} = E_{\text{rlx}}^{\text{sys}} - \left(E_{rlx}^{\text{CN}} + E^{Y}\right) \qquad \text{(Eq. S7)}$$

Here, $E_{\text{rlx}}^{\text{sys}}$ is the total energy of each system after relaxation, $E_{\text{rlx}}^{\text{CN}}$ is the relaxed energy of the CN surface and E^{Y} is the energy of an isolated Y atom on the surface.

This computational approach allowed us to systematically explore the interaction mechanisms and energetics governing the adsorption of yttrium on the carbon nitride surface, providing valuable insights into the surface-adsorbate interactions at the atomic scale.

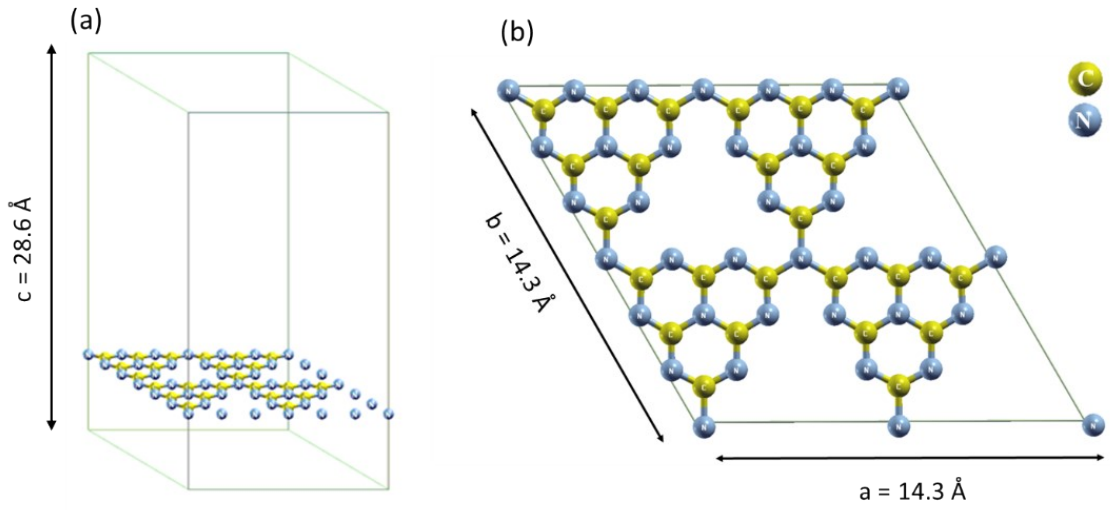

Fig. S17. Schematic model of the CN with tri-*s*-triazine geometry (ideal graphitic C_3N_4): (a) side-view, and (b) top-view.

The ion core is described by plane wave (PAW) pseudopotentials and the valance electrons (*2s2p* electrons for C and N atoms, *4s4p4d5s* electrons for Y atoms) are treated explicitly with a kinetic cut-off of 50 Ry for the wave function and 350 Ry for the charge density. The exchange-correlation potential is treated within the Perdew–Burke–Ernzerhof (PBE) generalized gradient approximation (GGA),[23] and according to Monkhorst and Pack scheme,[24] a *k*-mesh of 2 $\times$ 2 $\times$ 1 was constructed. All the relaxations were carried out until the residual forces of the atoms were less than 10^{-3} Ry B^{-3} and the change in energy was less than 5×10^{-5} Ry. A self-consistent convergence criterion of 10^{-6} Ry was imposed for the final relaxed structures, and an electron structure (electron density, density of states (DOS), and charge transfer by Löwdin population analysis) was computed.

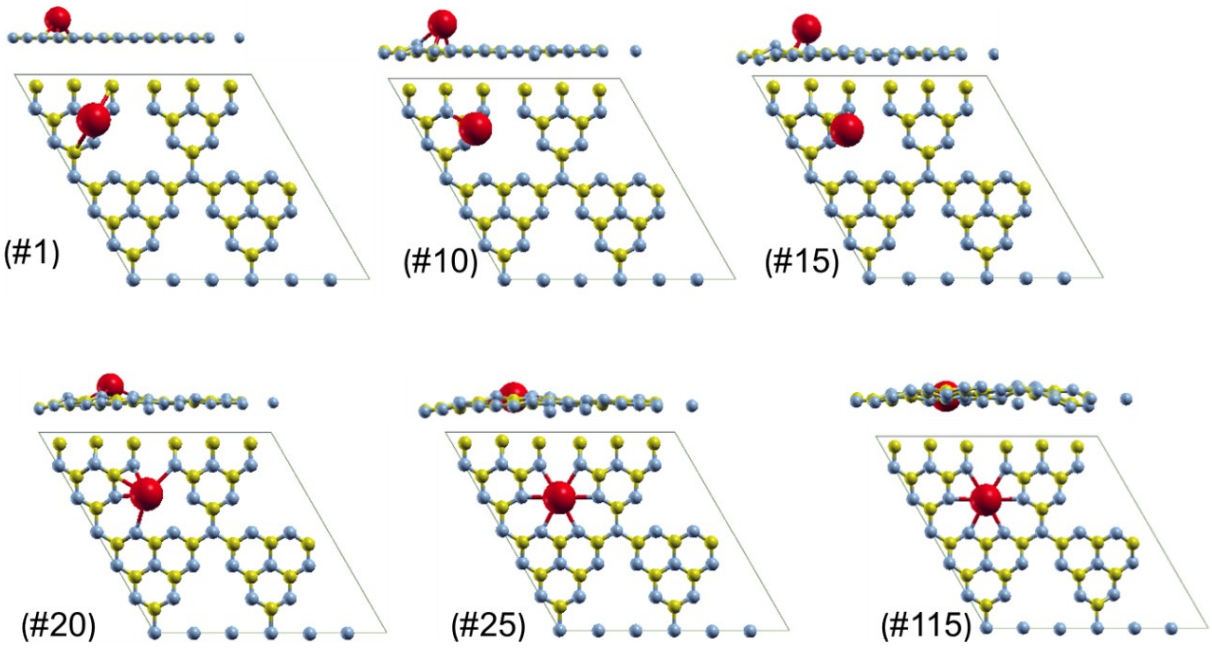

Fig. S18. Snapshots illustrate the side- and top-views of a representative yttrium (Y) atom as it undergoes the relaxation process. The yttrium atom is shown in its starting position in the initial relaxation step (step #1). As the relaxation progresses, the yttrium atom migrates toward the larger pores within the simulated single-layer CN structure.

Supplementary Information References

1 F. Aubriet, C. Poleunis, J. Muller and P. Bertrand, *J. Mass Spectrom.*, 2006, **41**, 527–542.

2 A. Tashakory, S. Mondal, V. R. Battula, G. Mark, T. Shmila, M. Volokh and M. Shalom, *Small Struct.*, 2024, **5**, 2400123.

3 S. Mondal, G. Mark, A. Tashakory, M. Volokh and M. Shalom, *J. Mater. Chem. A*, 2024, **12**, 11502.

4 D. Garg, T. Shmila, G. Mark, S. Mondal, V. R. Battula, M. Volokh and M. Shalom, *Adv. Sustain. Syst.*, 2024, **8**, 2300447.

5 C. Murugan, K. Ranjithkumar and A. Pandikumar, *J. Colloid Interface Sci.*, 2021, **602**, 437–451.

6 S. Mondal, T. Naor, M. Volokh, D. Stone, J. Albero, A. Levi, A. Vakahi, H. García, U. Banin and M. Shalom, *ACS Appl. Mater. Interfaces*, 2024, **16**, 38153–38162.

7 Y. Lei, W. Si, Y. Wang, H. Tan, L. Di, L. Wang, J. Liang and F. Hou, *ACS Appl. Mater. Interfaces*, 2023, **15**, 6726–6734.

8 J. Xia, N. Karjule, L. Abisdris, M. Volokh and M. Shalom, *Chem. Mater.*, 2020, **32**, 5845–5853.

9 S. Mondal, M. Salati, M. Nicaso, J. Albero, M. Segado-Centellas, M. Volokh, C. Bo, H. García, M. Gil-Sepulcre and A. Llobet, *Chem. Sci.*, 2024, **15**, 16546–16553.

10 Y. Wang, W. Si, H. Tan, Z. Xie, L. Wang, L. Di, J. Liang and F. Hou, *Sci. China Mater.*, 2023, **66**, 623–633.

11 G. Peng, J. Qin, M. Volokh, C. Liu and M. Shalom, *J. Mater. Chem. A*, 2019, **7**, 11718–11723.

12 F. Zhi, S. Wu, C. Lai, M. He, W. Deng, D. Zhang, X. Peng, Q. Wu, J. Xia and Z. Lu, *Small*, 2024, 2401123.

13 W. Zhang, J. Albero, L. Xi, K. M. Lange, H. Garcia, X. Wang and M. Shalom, *ACS Appl. Mater. Interfaces*, 2017, **9**, 32667–32677.

14 J. Zhang, Y. Zou, S. Eickelmann, C. Njel, T. Heil, S. Ronneberger, V. Strauss, P. H. Seeberger, A. Savateev and F. F. Loeffler, *Nat. Commun.*, 2021, **12**, 3224.

15 Y. J. Seo, P. K. Das, M. Arunachalam, K.-S. Ahn, J.-S. Ha and S. H. Kang, *Int. J. Hydrogen Energy*, 2020, **45**, 22567–22575.

16 S. Vinoth, W.-J. Ong and A. Pandikumar, *J. Colloid Interface Sci.*, 2021, **591**, 85–95.

17 M. Karimi-Nazarabad, E. K. Goharshadi and H.-S. Sajjadizadeh, *J. Phys. Chem. C*, 2022, **126**, 8327–8336.

18 Y. Liu, J. Zhang, X. Li, Z. Yao, L. Zhou, H. Sun and S. Wang, *Energy & fuels*, 2019, **33**, 11663–11676.

19 T. Shmila, S. Mondal, S. Barzilai, N. Karjule, M. Volokh and M. Shalom, *Small*, 2023, **19**, 2303602.

20 N. Karjule, C. Singh, J. Barrio, J. Tzadikov, I. Liberman, M. Volokh, E. Palomares, I. Hod and M. Shalom, *Adv. Funct. Mater.*, 2021, **31**, 2101724.

21 N. Karjule, J. Barrio, L. Xing, M. Volokh and M. Shalom, *Nano Lett.*, 2020, **20**, 4618–4624.

22 P. Giannozzi, S. Baroni, N. Bonini, M. Calandra, R. Car, C. Cavazzoni, D. Ceresoli, G. L. Chiarotti, M. Cococcioni and I. Dabo, *J. Phys. Condens. matter*, 2009, **21**, 395502.

23 J. P. Perdew, K. Burke and M. Ernzerhof, *Phys. Rev. Lett.*, 1996, **77**, 3865.

24 H. J. Monkhorst and J. D. Pack, *Phys. Rev. B*, 1976, **13**, 5188.